Research Article | Vol. 11, No. 9 / 1 September 2020 / Biomedical Optics Express 5003
Biomedical Optics EXPRESS

Longitudinal in-vivo OCM imaging of glioblastoma development in the mouse brain

HUBERT DOLEZYCZEK,[1,5] MOUNIKA RAPOLU,[2,5] PAULINA NIEDZWIEDZIUK,[2] KAROL KARNOWSKI,[2] DAWID BORYCKI,[2] JOANNA DZWONEK,[1] GRZEGORZ WILCZYNSKI,[1] MONIKA MALINOWSKA,[1] AND MACIEJ WOJTKOWSKI[2,3,4,6]

[1]*Nencki Institute of Experimental Biology, Polish Academy of Sciences, ul. Pasteura 3, 02-093 Warsaw, Poland*
[2]*Institute of Physical Chemistry, Polish Academy of Sciences, ul. Kasprzaka 44/52, 01-224 Warsaw, Poland*
[3]*Baltic Institute of Technology, Al. Zwycięstwa 96/98, 81-451 Gdynia, Poland*
[4]*Faculty of Physics, Astronomy and Informatics, Nicolaus Copernicus University, Gagarina 11, 87-100 Toruń, Poland*
[5]*both authors contributed equally*
[6]*mwojtkowski@ichf.edu.pl*

Abstract: We present in-vivo imaging of the mouse brain using custom made Gaussian beam optical coherence microscopy (OCM) with 800nm wavelength. We applied new instrumentation to longitudinal imaging of the glioblastoma (GBM) tumor microvasculature in the mouse brain. We have introduced new morphometric biomarkers that enable quantitative analysis of the development of GBM. We confirmed quantitatively an intensive angiogenesis in the tumor area between 3 and 14 days after GBM cells injection confirmed by considerably increased of morphometric parameters. Moreover, the OCM setup revealed heterogeneity and abnormality of newly formed vessels.

1. Introduction

Almost all of the primary and essential biological functions of developed living organisms (e.g., breathing, heartbeat, sleep, etc.) are controlled by the brain - center of the nervous system. Several millions of people around the world are affected each year due to medical conditions like stroke, tumor, neurological disorders, which can be interrelated affecting the brain and the same on the activity of the entire organism. There is only a limited state of art imaging techniques that can penetrate through skull like computed tomography (CT), positron emission tomography (PET), magnetic resonance imaging (MRI).

In vivo, optical imaging is still an extremely difficult challenge due to the highly scattering properties of the skull and the relatively high optical density of the brain's cortex itself. While the first problem is still unresolved, the maintenance of relatively deep brain penetration above 3 mm and high spatial resolution has been demonstrated by using optical coherence tomography (OCT) [1]. OCT is a non-invasive technique that uses near-infrared light to optimize competing resolution and penetration depth parameters. OCT also provides the advantage of 4-D information on brain dynamics without using exogenous contrasting agents [2]. These advantages make OCT techniques unique and useful for monitoring tumor progression in the brain, as typically, the tumor scattering properties increase during longitudinal progression resulting in a reduced depth of imaging for methods using visible light such as confocal microscopy or fluorescence imaging [3]. Optical coherence microscopy (OCM) circumvents some of the limitations of optical coherence tomography (OCT) with achieving the micron-scale transverse resolution, especially vital in biological tissue imaging [4,5]. In turn, optical coherence angiography (OCTA) is an OCT modality that enables to access function of the sample like visualization of the microvasculature

#400723 https://doi.org/10.1364/BOE.400723
Journal © 2020 Received 18 Jun 2020; revised 30 Jul 2020; accepted 4 Aug 2020; published 12 Aug 2020

Biomedical Optics EXPRESS

structure in the biological specimen in addition to the structural information. High-resolution OCTA can be achieved with high sampling density yielding additional information of depth-resolved vasculature from large vessels down to capillaries (2-10 um) using the dynamic motion properties of the red blood cells (RBC's) in vessels [6–10]. The combination of both OCM and OCTA gives the information of enface, structural information, vessels, capillaries, vasculature map, and morphology at the cellular level.

Glioblastoma multiforme (glioblastoma, GBM) is the most common primary malignant brain tumor in humans. According to the World Health Organization (WHO) classification, this glioma is characterized by the highest, the fourth grade of malignancy (G-IV), which means the survival of patients on average below two years [11]. Molecular and cellular heterogeneity of the glioblastoma cells, infiltration, and rapid proliferation, supported by the intense development of the network of blood vessels of the tumor (angiogenesis), affect the resistance to treatment. Despite the development of innovative diagnostic strategies and new therapy, the prognosis for patients with glioblastoma multiforme is still bad [12]. Several animal glioma models were developed to understand the pathomechanism of the human glioma [13,14]. One of the most frequently used is based on GL-261 glioma cells for tumor development. Primarily GL-261 was induced *in-vivo* by intracranial injection of 3-methylcholantrene into C57/BL6 mice [15]. The GL-261 glioma model displays many characteristic histological and biological features of human glioblastoma multiforme. The tumor is solid, has a repeatable internal structure, which will ensure repeatability of observation and comparison with literature data. Due to intensive GL-261 cell proliferation, the tumor multiplies, which shortens the time of the experiment and the suffering of animals [16].

The ability to distinguish the GBM tumor tissue from healthy tissue structurally, morphologically, and optically has already been demonstrated using OCT by several research groups [17–20]. *Ex-vivo* studies on different types and grades of glioma tumor showed the potential of OCT to detect, identify, and discriminate both glioma and meningioma [21]. A study comparing three different OCT systems for both ex-vivo and in-vivo clinical studies have demonstrated the imaging capability to distinguish brain tissue from healthy tissue using the attenuation coefficient as the primary differentiation factor [22]. A recent study from glioma, both ex-vivo and in-vivo studies using cross-polarization OCT (CP OCT), which uses the polarization properties of the tissues, could be able to distinguish normal from tumorous by visual assessment of CP OCT images [23]. In neurosurgery, the capability to apply the improved extent of resection of the brain tumor tissue is demonstrated using OCT [24–28]. Most of these studies lack angiography information, which reveals the tumor microvasculature. To evaluate the tumor microenvironment and response to therapy in the mouse brain, a Fourier domain Swept Source OCT approach (called alternatively as OFDI) was used to achieve wide-field, a higher resolution with a large depth of focus [29]. There are a very few experimental reported studies of OCT-angiography (OCTA) used to access microvasculature of the *in-vivo* GBM tumor in the brain [28–32]. OCTA and OCM have been already used for in-vivo brain imaging to study stroke models and other functional changes by several research groups [33–42]. Although the Doppler OCT can additionally visualize the flow of blood and quantify the flow velocity, it is limited only to large vessels [43,44]. This would not be relevant in studying small tumor growth. All of the previous studies lack the systematic longitudinal analyses and quantification of the GBM tumor growth progression based on OCTA data. There is still a significant gap and need in understanding vascularization, angiogenesis, changes in microvasculature/blood vessels, tissue morphology, and tumor response during the longitudinal growth process. This is also important to track the physiological and pathological dynamic changes.

It is essential to quantify the growth of a brain tumor, which is a necessary step i*n- vivo* longitudinal studies. Unlike *ex vivo* studies in which the mouse is euthanized at each stage, we assume the possibility of minimally invasive imaging of structural or functional changes of the

Biomedical Optics EXPRESS

malignant area over time. This study focuses on the quantitative and qualitative analysis of the longitudinal progression of angiogenesis accompanying the growth of GBM tumors. The advantage of our method is to keep the brain functionally undisturbed by using a transcranial window and by keeping the dura intact, giving an insight into the tumor under real conditions [45]. To the best of our knowledge, the presented results are the first in the world to show the monitoring of changes in cerebral microcirculation during the growth of a GBM tumor in the brain up to 2 weeks using OCTA. We quantified the tumor with a set of vascular parameters obtained by fractal analysis. Thanks to this work, we have taken the first step towards biomarkers, which enable quantitative analysis of GBM development. During these studies, intensive angiogenesis was found in the tumor area between 3 and 14 days after GBM cell injection, confirmed by considerably increased morphometric parameters. Moreover, the OCM system showed heterogeneity and abnormalities of newly formed vessels.

2. Materials and methods

2.1. Experimental setup, scanning protocol, and data analysis

In this study, we used spectral OCM system based on a Michelson interferometer configuration (Fig. 1). We used a ~6fs short pulse laser light along with a 75:25 fiber beam splitter to split the output into the reference and the object arm, respectively. The reflected light from the sample and the reference mirror was coupled using a fiber coupler and directed into a spectrometer. To provide a high axial resolution of 2.2 µm, a femtosecond laser (Fusion Femtolasers, Austria) centered at 795 nm with 130 nm full bandwidth was used as a light source. The interferometric signal was recorded by a custom-made spectrometer with 2048 pixels of high-speed line scan camera (Basler Sprint, Germany). Interchangeable imaging optics can be used with the OCM system; however, for this study, we used a 4x microscope objective (Olympus Plan Fluorite, NA = 0.13, equivalent full aperture = 11.7 mm, effective focal length = 45 mm, maximum transverse resolution at 800nm = 2.5 µm). To compromise between lateral resolution and depth of focus the beam entering the objective was expanded to 6 mm (at $1/e^2$ of the Gaussian profile) by achromatic lenses L_3=30 mm and L_4=100 mm [Fig. 1(A)]. The theoretically estimated confocal parameter is ~100 µm for obtained transverse resolution of $\Delta x = 4.5$ µm (at FWHM of Gaussian profile). The sample was illuminated with 10 mW average optical power. A-scans were collected at 50 kHz repetition rate. Three dimensional volumes covering area of 2.8×2.8 x 2 mm^3 were acquired with sampling density of $800 \times 800 \times 2048$ pixels for X, Y and Z axis respectively. For better visualization of the Region of Interest we cropped the volumetric data to 1.7 mm x 1.7 mm x 0.4 mm containing $400 \times 400 \times 400$ pixels. The 2mm measuring range of the OCT was selected to facilitate the positioning of the mouse brain and to be able to react during the measuring session to accidental movements of the animal. At each position along Y-axis, the B-scans were repeated six times with a repetition time of 8.2 ms. Such six repeated frames were used to calculate angiographic cross-sections or averaged to improve the quality of OCT structure images. Full 3D volume was collected within 19.2 s, but total measurement time – including data transfer and saving - was 94s. Dedicated stand-alone software, developed in LabView, allowed the control of a scanning protocol, synchronization of camera and scanners, and data processing. Data analysis enabled the volumetric reconstruction of mouse brain structure as well as angiographical mapping.

The pre-processing included standard steps for OCT systems: spectrum linearization in *k-space*, numerical dispersion correction, and fast fourier transform. Complex valued data was either averaged (N = 6) to provide high-quality structure information, or processed towards the visualization of brain vasculature. OCT angiographic processing was based on the absolute complex difference (ACD) method in Fig. 1(B) that for mouse brain imaging provides the best angiographic contrast, especially for the smallest capillaries [36]. All 6 B-scans acquired at a given Y location were first corrected for potential bulk motion. Then ACD was calculated as

Biomedical Optics EXPRESS

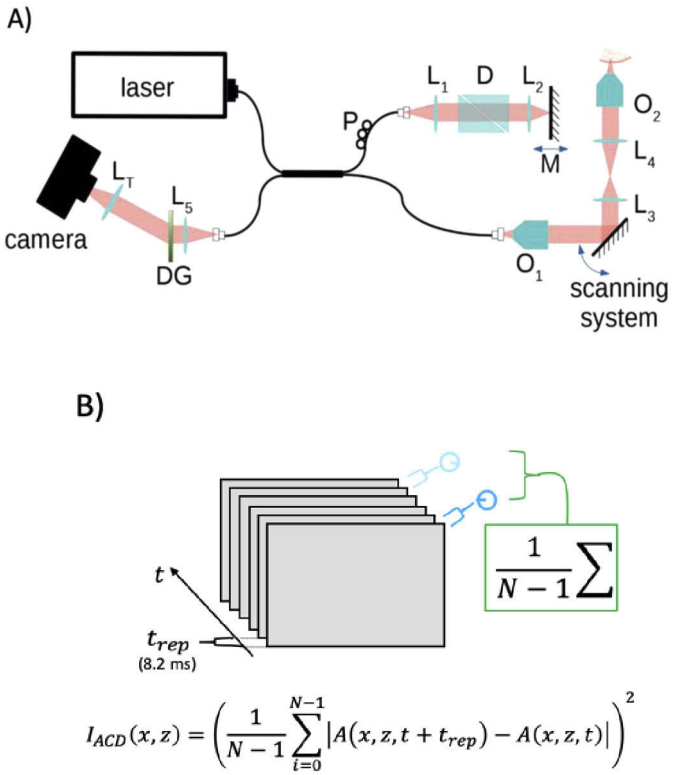

Fig. 1. a) Schematic drawing of the OCM setup: L_{1-5} - achromatic doublet lenses (f: 250 mm, 100 mm, 30 mm, 100 mm, 50 mm respectively); L_T - telecentric lens, f = 80 m; DG - diffraction grating; $O_{1,2}$ – objectives 20x with 0.4NA and 4x with 0.13NA respectively; M – mirror; D - dispersion compensation module; P - polarization controller. b) The Absolute complex difference method used to obtain the angiographic images.

an amplitude of complex difference between consecutive pair of B-scans and further averaged over 5 of such pairs. The procedure was repeated for all Y axis locations and presented either as angiographic B-scans or *en-face* angiographic projections by taking maximum intensity along Z-axis. We extracted various morphological parameters from OCM *en-face* angiographic projections to estimate the progress of angiogenesis during tumor growth. The region of interest (ROI), of the same diameter for all time points, was identified for both Glioma and control datasets as a circular region around the injection area. The choice of the ROI was dictated by the shape of the changes introduced by the application of culture medium in the control group. We assumed that the potential protocol for monitoring tumor progression would typically be assisted by the control group to quantify the immune response to the cell injection objectively. Further, we applied a multi-scale Frangi-Hessian filter, which enhances the tube-like structures to extract only vascular information and to segment the vasculature for quantitative analysis [46]. The vessels (sigma) of the filter, which signifies the vessel diameter was adjusted to match the original vasculature size. The AngioTool (National Cancer Institute) and post-processing were made in Python to parameterize and quantitatively access the morphometric and vessel parameters like vessel area, total vessel length, number of junctions, and number of endpoints. The parameters are defined as follows:

(i) "Vessel Area" relates to the total area of the segmented vessels.

Biomedical Optics EXPRESS

(ii) "Total Number of Junctions" represents all vessel's bifurcations.

(iii) "Total Vessels Length" describes the total Euclidian distance of all the vessels calculated between pixels in the image.

(iv) "Total Number of End Points" is the total number of only open-ended segments present [47].

These angiometeric parameters estimate the quantitative and qualitative information about the growth of the tumor.

2.2. Animals

All procedures performed according to the rules established by the First Local Ethical Committee on Animal Research in Warsaw. These rules are based on national laws in full accordance with the European Union directive on animal experimentation.

2.3. Glioblastoma cell preparation

GL-261 cells were obtained from the Division of Cancer Treatment and Diagnosis (DCTD) Tumor Repository, National Cancer Institute (NCI), Frederick, Maryland. After thawing, cells were cultured in DMEM medium, supplemented with 10% Fetal Bovine Serum (FBS), 1% L-glutamine, and 1% penicillin/streptomycin on T75 flask. The cell line was maintained at a constant temperature of 37°C with a CO_2 level of 5%. When the culture reached 80-100% confluence, the cells were trypsinized with 0,05% trypsin and neutralized with culture medium. Before implantations, floating cells were centrifuged, suspended in culture media to appropriate concentration, and maintained on ice for immediate injection.

2.4. GL-261 cell injection and cranial window implantation

C57BL/J6 mice (age 6–10 weeks old, weight 20–25 g) were used in the experiments. Two mice were used for GL-261 implantation (M1, M2), and two served as a control (M3, M4). To prepare the mice for OCM imaging, a cranial window was implanted over the parietal-temporal lobe and centered on the barrel cortex of the right hemisphere. The cranial window was located at 2.5 mm posterior to bregma. The mice have been placed in a stereotaxic frame and deeply anesthetized with isoflurane (4% for induction; 1.5–2% for surgery). Dexamethasone (0.2 mg/kg) and Carprofen (5 mg/kg) were administered subcutaneously to prevent an inflammatory response and brain edema. A warming pad with an anal probe containing an automated temperature control feedback system was used for monitoring body temperature (maintained at 37 °C level during surgery). After removing the skin over the top of the skull, a drop of 1% lidocaine: epinephrine ($1{:}10^5$) solution was applied onto the periosteum to avoid excessive bleeding or pain. A circular portion of the skull (diameter 4 mm) was removed to expose the dura mater. The dura mater was incised, and 5×10^3 GL-261 cells in 0,3 µl culture medium were injected with Hamilton syringe (Fig. 2, d0) to depth of 300-800 microns into the somatosensory cortex. Control mice were injected with the cell culture medium only to the same depth. Then the brain surface was covered with 0.9% NaCl and a cover glass (diameter 5 mm) was attached with cyanoacrylate-based glue and sealed with dental acrylic. After the surgical procedure, the mice were transferred to cages and monitored until total recovery. Figure 2 demonstrates the glioma cell injection procedure and tumor appearance and growth across 14 days.

2.5. In-vivo OCT imaging

OCM measurements were acquired at 1, 3, 11, 14 days from G261 implantation and the injection of the cell culture medium. Each animal is placed in a stereotaxic frame with a warming pad and was deeply anesthetized with isoflurane (4% for induction; 1.5–2% for the procedure). The

Biomedical Optics EXPRESS

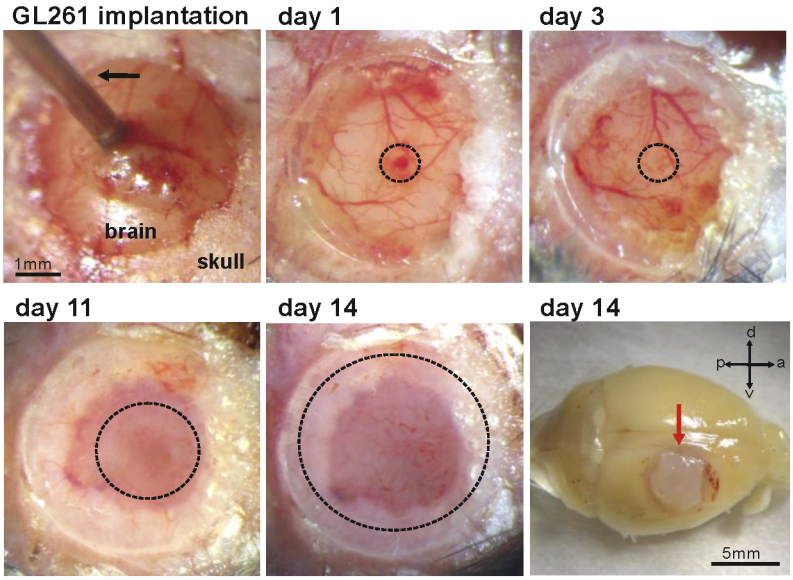

Fig. 2. Implantation of GL-261 cells into the mouse cortex. Black arrow points on the needle of Hamilton syringe used for delivery of the cells. Dotted circle on photographs day 1 – day 14 shows approximate borders of growing tumors. On the right bottom picture (day 14) is shown mouse brain with visible tumor – red arrow (d – dorsal, v – ventral, p – proximal, a – anterior).

stereotaxic frame was then positioned in the sample arm of the OCM setup using a custom-made three-axis platform. Cranial window enabled OCM *in-vivo* imaging of the animal's brain. The gaussian OCM imaging system with long working distance (7.5 mm) of the 4x objective lens yielded an advantage of precise and comfortable animal positioning. The scanned region have a field of view (FoV) of $2.8 \times 2{,}8 \times 0.4$ mm and 1.7 mm x 1.7 mm x 2 mm in XYZ axes. The structural B-scan transformation produced the following images: phase-variance (angiographic) B-scans, structural, and angiographic *en-face* projections of the imaged region.

2.6. Histology

Histological hematoxylin-eosin (HE) staining was performed 14 days after GL-261 cell implantations. The mice were anesthetized with pentobarbital and perfused with warm (37 °C) phosphate-buffered saline (PBS) for 5 min, followed by 4% paraformaldehyde in PBS for 15 min (at room temperature). The brains were postfixed overnight in the same fixative solution and impregnated in 30% sucrose for 3-5 days. Next, mouse brains were cut on cryostat into serial coronal sections with 40 µm thickness. The sections were mounted on SuperFrost (Fisher Scientific, Hampton, New Hampshire /USA) slides, air-dried on a slide warmer at 58 °C for at least 30 min. Following this, the sections were hydrated in tap water, then stained in Mayer's hematoxylin (Diapath, Martinengo, Italy) for 6 min, and washed in running tap water for 5 min. Next, the slides were stained in Shandon Eosin Y (Thermo Fischer Scientific, Waltham, Massachusetts, USA) for 2 min, washed in tap water for 2 min, dehydrated in baths with increasing alcohol concentrations (1 min in each bath of 50%, 80%, 90% and 100% ethanol), and cleared in xylene. Finally, the sections were mounted in Shandon Consul-Mount media (Thermo Fischer Scientific), a non-aqueous, non-fluorescent plastic mounting media.

Biomedical Optics EXPRESS

3. Results

To completely confirm the presence of a malignant brain tumor after cell implantation, we evaluated the structure and size of glioma tumor based on histology (HE staining) and compared it to structural OCM reconstructions. After 14 days of glioma growth, histology revealed intense violet staining of the tumor with hematoxylin, clearly darker than the surrounding tissue (Fig. 3). The size of the tumor was approximately 1.8 mm x 2 mm x 3 mm (length, width, and depth, respectively). The tumor occupied the cortex's entire thickness with part of the lateral ventricle [Fig. 3(b), 3(c)].

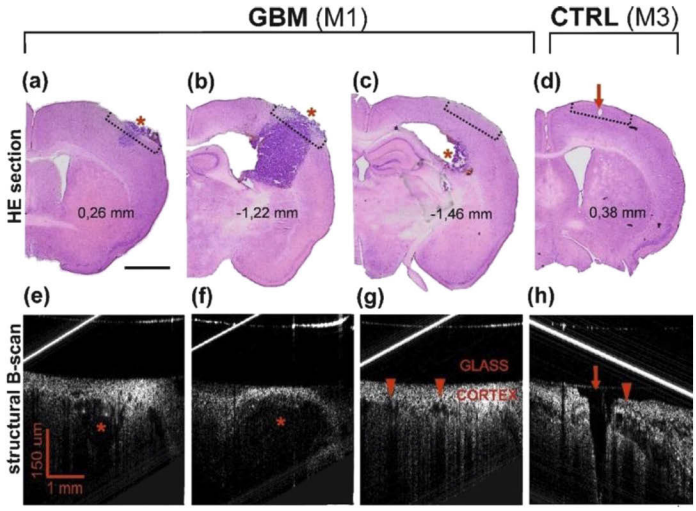

Fig. 3. Structure of the glioblastoma tumor in the mice cortex on the 14th day of the tumor growth. (a-c) HE coronal sections showed the tumor's appearance at the anterior-posterior levels: 0,26 mm, −1,22 mm, and −1,46 mm from bregma; scale bar = 2 mm. The red stars show tumor location. (d) HE stained coronal section of the control mouse on the 14th day (the red arrow shows the space where the cell culture medium was injected); (e-h) Structural B-scans took at the corresponding levels of HE sections; area of the scanned region is presented by black dotted lines on (a-d); red arrowheads show the signal from vessels in healthy tissue, the red arrow in the panel (h) shows the space created after injection of the medium in the control mice.

Structural OCM B-scans also revealed a characteristic structure of the glioma, visible as a hyporeflective signal area surrounded by the bright scattered signal of neighbor healthy tissue [Figs. 3(e), 3(f)]. Larger vessels surrounding the tumor can be easily identified in the structural OCM images and are seen on the cross-sections as a "butterfly pattern" with a dark shadow signal below [Fig. 3(g)]. A different pattern of scattering signal was obtained for the control mouse injected with the cell culture medium. Figure 3(d) shows the needle trace surrounded by HE stained healthy tissue, and Fig. 3(h) shows the corresponding structural B-scan.

To follow up on the tumor progression, the OCM measurements were taken over two weeks period at the following time points: 1, 3, 11, and 14 days after injection of the glioma cells. The areas where glioma cells (day 1) or the control culture medium (day 3 and 14) were injected are visible on OCM, both angiographic and structural *en-face* projections. In both cases, the affected area is avascular and similar in size [Figs. 4(a)–4(f)]. The Field of view (FoV) in Figs. 4(a)–4(j) are of $2.8 \times 2.8 \times 0.4$ mm in XYZ axes. Between day 3 and day 11, is observed intense, significant tumor growth with a marked increase of vascular density. The tumor margin cannot be easily delineated based only on en-face OCM structural or angiographic images. However, we can

Biomedical Optics EXPRESS

estimate its size by looking at cross-sectional images [Fig. 5(f)] where we can identify growing hyporeflective areas. Based on complementing cross-sectional images and *en-face* images, we delineated potential tumor extend (average diameter of the tumor: day 3–0,6 mm; day 11–2,0 mm; day 14–2,3 mm), presented on *en-face* images by dotted yellow lines visible in Figs. 4(g)–4(l). Additionally, on day 14, we observe tumor expansion beyond the large vessel, which formed the physical barrier already visible on structural *en-face* projections [Figs. 4(j), 4(l), red arrows]. During tumor growth, we observed the progression of angiogenesis visible at day 14 [Fig. 4(k)] compared to day 11 [Fig. 4(i)]. Panels m and n in Fig. 4 also shows the OCTA data for two mice that had a tumor. In both cases we observed quite similar neovascularization process which led to the formation of irregular, tortuous and tangled microvasculature morphologically in the area of tumor proliferation.

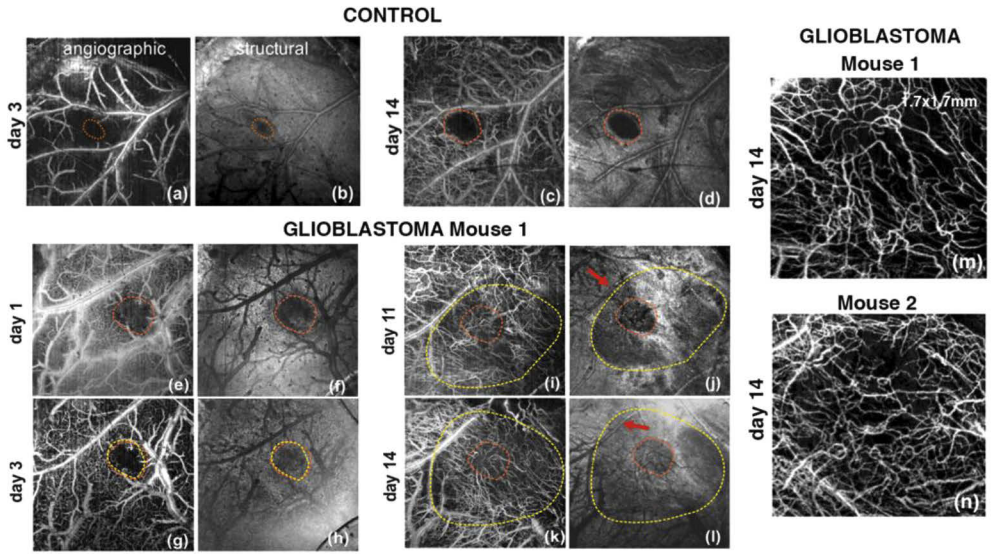

Fig. 4. Monitoring of glioblastoma tumor progression: OCM angiographic (a,c,e,g,i,k) and structural (b,d,f,h,j,l) en-face projections (transverse dimensions of 2.8×2.8 mm) taken at the selected time points showing progression of glioblastoma tumor development. The red dotted line indicates the needle trace. The yellow dotted line indicates the border of the tumor. Red arrow indicates the middle cerebral artery; Comparison of angiogenesis occurring in two mice used for tumor studies -angiographic OCM projections were zoomed to visualize irregular, tortuous and tangled microvasculature morphologically in the area of tumor proliferation (m,n).

We assessed the diversity of the tumor structure and vasculature at various cortical depths after 14 days of GBM development. In the first superficial layer (0-50 um below the surface), we observed the highest density of newly formed thin meningeal vessels with loops characteristic for tumor [Fig. 5(a)]. The Field of view (FoV) for the angiomaps in Figs. 5(a)–5(d) is $2.8 \times 2.8 \times 0.4$ mm in XYZ axes. In the deeper layer (50-100 um), there were evidently fewer vessels visible within the tumor, due to increased degeneration in this region. Deepest layers that were analyzed (100-200 um and 200-300 um) reveal maps of rare radially arranged, tortuous vessels. Vascularization abnormality was confirmed on HE stained sections of the glioma [Fig. 6(b)]. The healthy tissue closely surrounding the glioma area contains much narrower and more numerous vessels [Fig. 6(a)].

To assess the angiogenesis quantitatively in the tumor region, we performed an analysis of morphological parameters characterizing the vessel network (vessel area, total number of

Biomedical Optics EXPRESS

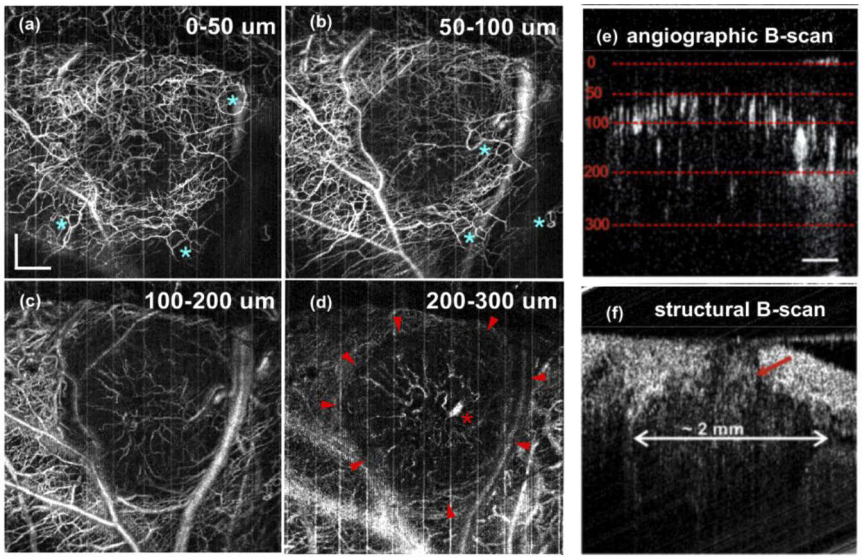

Fig. 5. OCM images of vascularity and structure of the GBM tumor after 14 days in mouse M1. (a-d) angiomaps with dimensions of 2.8×2.8 mm presenting blood vessels taken from four depths; (a) 0-50 um, (b) 50-100 um, (c) 100-200 um, (d) 200-300 um. Blue stars depict specific for glioma loops of newly formed vessels; red star indicates another abnormality of vessel appearance; red arrowheads delimit border of the tumor. (e) Angiographic B-scan (2.8×0.4 mm) reveals signals from vessels with blood flow on different depths of the tumor area. (f) Structural B-scan (2.8×0.4 mm) demonstrates scattering signal characteristics for the tumor. The red arrow shows a needle trace where glioma cells were delivered.

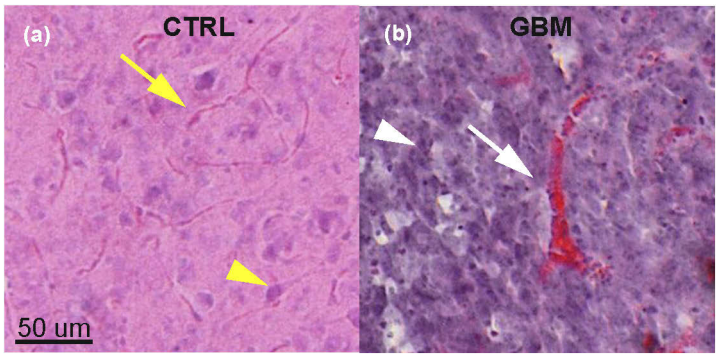

Fig. 6. HE stained the mouse cortex on average and GBM tissue (M1). (a) The yellow arrow indicates healthy capillaries; yellow arrowhead shows cortical neurons. (b) White arrow indicates abnormal dilated GBM vessel; white arrowhead shows GBM cell. Images obtained with 100x magnification.

junctions, total vessels Length, total number of endpoints) presented on *en-face* angiographic projections (Fig. 7). Selected areas [ROI, Region of Interest, Fig. 7(a)] for initial days (1-3) are avascular and analyzed parameters at low levels, similar for glioma and control groups. The diameter of the avascular region in ROI was around ~0.7 mm. On day 11, we observed a dramatic increase in all of the parameters indicating potent angiogenesis. Further increase of parameters was observed for day 14. All characterization parameters for the control mice remained at low levels over the whole investigation period [Fig. 7(c)].

Biomedical Optics EXPRESS

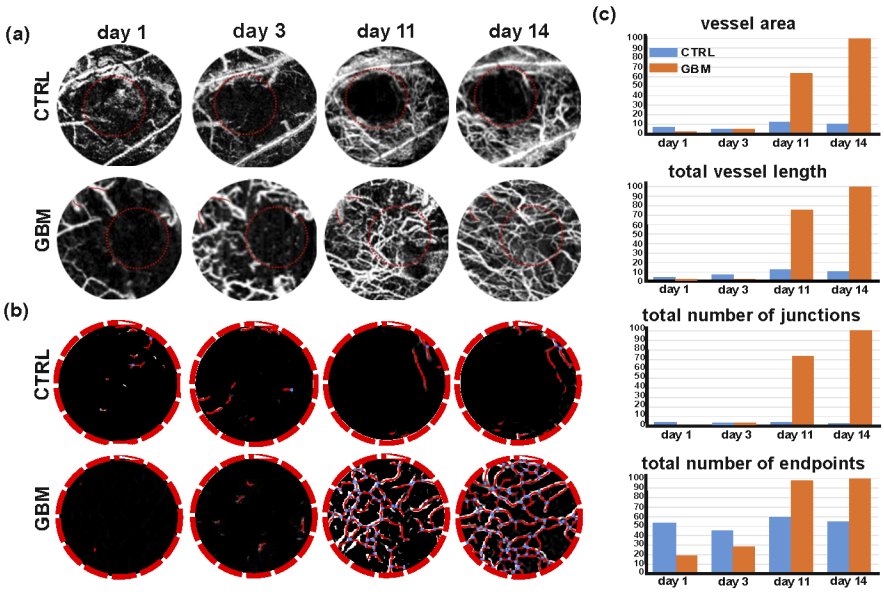

Fig. 7. Analysis of the vascularity in the Glioblastoma (GBM) tumor region at day 1, 3, 11, and 14 in M2. (a) Angiomaps with a red dotted circle (ROI) indicating region chosen for analyses. (b) ROI after applying the Frangi-Hessian filter and the Fractal transformation. The blue dots represent the junctions, and the red curves indicate vessels. (c) Measurements of four parameters characterizing vasculature of the tumor in comparison to the control.

4. Discussion

The specificity of *in vivo* OCM imaging of mice is associated with some disadvantages. First of all, to obtain a good quality image, it is necessary to immobilize the animal's head, as the breathing movements interfere with the scattering signal. There is also the possibility of unexpected death of the animal due to the rapidly growing tumor and its expansion deep into the brain, therefore it is necessary to monitor the physiological state of the mice throughout the experiment. The applied method of the GL-261 line cell implantation allowed for the precise, repeatable location of the tumor, and placement of the cells into the deep layer of the cortex was necessary to obtain solid tumors. Side effects of the method were tissue and vessel damage in the area of needle insertion, which caused the OCM images to be obscured in the first days of tumor development.

The widely recognized and used method of brain imaging through the cranial window [48,49] has enabled long-term observation of the tumor area; however, it causes astrocytosis and associated inflammation, lasting up to 3 months [45,50] Another study showed that the scattering signal was significantly correlated with the level of astrocytosis in the borderline of the infarction [47].

On the first day, we injected a suspension of glioblastoma cells into the cortex with a Hamilton syringe (needle diameter approximately 1mm), then the brain tissue was covered with glass and glued to the bone. All of these activities cause irritation of brain tissue, including the numerous micro-hematomas shown in Fig. 1 (day 1), and the leakage of a small portion of the glioblastoma cell suspension on the brain surface. It seems to us that all this disturbs the penetration of tissue by the laser beam and disturbs the scattering signal, which results in a lower quality, blurred OCM images on the day 1. Also, the immune response was individually variable. In some cases the inflammation was so high that its effects made it completely impossible to imaging the blood vessels and monitor the tumor progression.

Biomedical Optics EXPRESS

5. Summary

As a result of OCM measurements, we obtained structural and angiographic images that characterize the tumor structure and vascularization. Glioblastomas are highly vascularized tumors characterized by an abundance of disorganized microvessels with chaotic organization. Highly dense regions neighbor vessel-poor areas, and vessels vary from a normally wide, irregular, and tortuous serpentine-like shape [51] what is in agreement with our observation of rare, radially arranged, tortuous vessels. In both structural B-scans and *en-face* projections, the tumor boundary was visible due to weaker scatter signal in the tumor area. Similarly, tumor margin was easily detected using cross-polarization OCT (CP OCT) in the rat model [52] and the mouse model using speckle-modulating OCT (SM-OCT) [53]. An attempt to identify the tumor border was made on sections of the human brain after intraoperative resection of glioma [23]. Thus, OCM imaging seems useful in determining the changes in the size of the tumor in the course of its growth. This parameter can be critical to assess the effectiveness of experimental cancer therapy.

Up to today, they are no OCM studies available related to analyzing quantitatively *in-vivo* neovascularization in glioblastoma development. On the other hand, the advantage of OCT in 3D imaging of sprouting of newly formed vessels in vitro has been shown [54]. Besides, OCT techniques were used in ophthalmology to diagnose neovascularization in macular degeneration [55,56].

Our OCM system is characterized by high resolution (2-3um), which allows on an accurate assessment of cerebral vascularization. It enabled us to show the tumor neovascularization progress visible on the obtained angiomaps. However, the quantitative parameters usually used to assess angiogenesis do not give high specificity due to large individual variability in vascular morphology. In our case, we have taken advantage of the elementary fact that in most of the pharma applications, it is necessary to run a control group in which the region of cell implantation remains changed for a few days after the start of the procedure. Thanks to this, we were able to show that each of them (not very sophisticated) parameters determining the state of blood vessels shows specificity. Therefore, we could confirm the neovascularization process quantitatively based on morphometric features, which demonstrated multiple increases in vessel area, total vessel length, number of junctions, and number of endpoints compared to low constant values in these parameters in control. Additionally, we confirmed the diversity of the vessel structure within the glioma in the mouse brain by histological staining.

Funding

Fundacja na rzecz Nauki Polskiej (MAB/2019/12); H2020 Spreading Excellence and Widening Participation (666295); Baltic Institute of Technology - commercialization of innovative solutions in economic practice co-financed by the Municipality of the City of Gdynia (contract No. 3 / DOT / 2016); Narodowe Centrum Nauki (2015/17/B/NZ4/02540); Ministerstwo Nauki i Szkolnictwa Wyższego (International co-financed project).

Disclosures

The authors declare that there are no conflicts of interest related to this article.

References

1. S. P. Chong, C. W. Merkle, D. F. Cooke, T. Zhang, H. Radhakrishnan, L. Krubitzer, and V. J. Srinivasan, "Noninvasive, in vivo imaging of subcortical mouse brain regions with 1.7 μm optical coherence tomography," Opt. Lett. **40**(21), 4911–4914 (2015).
2. K. Karnowski, A. Ajduk, B. Wieloch, S. Tamborski, K. Krawiec, M. Wojtkowski, and M. Szkulmowski, "Optical coherence microscopy as a novel, non-invasive method for the 4D live imaging of early mammalian embryos," Sci. Rep. **7**(1), 4165 (2017).
3. E. A. Genina, A. N. Bashkatov, D. K. Tuchina, P. A. Dyachenko Timoshina, N. Navolokin, A. Shirokov, A. Khorovodov, A. Terskov, M. Klimova, A. Mamedova, I. Blokhina, I. Agranovich, E. Zinchenko, O. V. Semyachkina-Glushkovskaya,

Biomedical Optics EXPRESS

and V. V. Tuchin, "Optical properties of brain tissues at the different stages of glioma development in rats: pilot study," Biomed. Opt. Express **10**(10), 5182–5197 (2019).
4. D. Huang, E. A. Swanson, C. P. Lin, J. S. Schuman, W. G. Stinson, W. Chang, M. R. Hee, T. Flotte, K. Gregory, and C. A. Puliafito, "Optical coherence tomography," Science **254**(5035), 1178–1181 (1991).
5. A. F. Fercher, C. K. Hitzenberger, G. Kamp, and S. Y. El-Zaiat, "Measurement of intraocular distances by backscattering spectral interferometry," Opt. Commun. **117**(1-2), 43–48 (1995).
6. J. K. Barton and S. Stromski, "Flow measurement without phase information in optical coherence tomography images," Opt. Express **13**(14), 5234–5239 (2005).
7. Y. Aizu and T. Asakura, "Bio-speckle phenomena and their application to the evaluation of blood flow," Opt. Laser Technol. **23**(4), 205–219 (1991).
8. J. D. Briers, "Speckle fluctuations and biomedical optics: implications and applications," Opt. Eng. **32**(2), 277–284 (1993).
9. A. Mariampillai, B. A. Standish, E. H. Moriyama, M. Khurana, N. R. Munce, M. K. Leung, J. Jiang, A. Cable, B. C. Wilson, and I. A. Vitkin, "Speckle variance detection of microvasculature using swept-source optical coherence tomography," Opt. Lett. **33**(13), 1530–1532 (2008).
10. A. Mariampillai, M. K. Leung, M. Jarvi, B. A. Standish, K. Lee, B. C. Wilson, A. Vitkin, and V. X. Yang, "Optimized speckle variance OCT imaging of microvasculature," Opt. Lett. **35**(8), 1257–1259 (2010).
11. K. Urbańska, J. Sokołowska, M. Szmidt, and P. Sysa, "Glioblastoma multiforme–an overview," Contemp. Oncol. (Pozn) **18**(5), 307–312 (2014).
12. M. Y. Lombardi and M. Assem, "Glioblastoma genomics: a very complicated story," in *Glioblastoma [Internet]* (Codon Publications, 2017).
13. S. Doblas, T. He, D. Saunders, J. Hoyle, N. Smith, Q. Pye, M. Lerner, R. L. Jensen, and R. A. Towner, "In vivo characterization of several rodent glioma models by 1H MRS," NMR Biomed. **25**(4), 685–694 (2012).
14. M. Miyai, H. Tomita, A. Soeda, H. Yano, T. Iwama, and A. Hara, "Current trends in mouse models of glioblastoma," J. Neuro-Oncol. **135**(3), 423–432 (2017).
15. J. I. Ausman, W. R. Shapiro, and D. P. Rall, "Studies on the chemotherapy of experimental brain tumors: development of an experimental model," Cancer Res. **30**, 2394–2400 (1970).
16. T. Szatmári, K. Lumniczky, S. Désaknai, S. Trajcevski, E. J. Hídvégi, H. Hamada, and G. Sáfrány, "Detailed characterization of the mouse glioma 261 tumor model for experimental glioblastoma therapy," Cancer Sci. **97**(6), 546–553 (2006).
17. A. Giese, H. Böhringer, J. Leppert, S. Kantelhardt, E. Lankenau, P. Koch, R. Birngruber, and G. Hüttmann, "Non-invasive intraoperative optical coherence tomography of the resection cavity during surgery of intrinsic brain tumors," in *Photonic Therapeutics and Diagnostics II*, (International Society for Optics and Photonics, 2006), 60782Z.
18. C. Kut, K. L. Chaichana, J. Xi, S. M. Raza, X. Ye, E. R. McVeigh, F. J. Rodriguez, A. Quiñones-Hinojosa, and X. Li, "Detection of human brain cancer infiltration ex vivo and in vivo using quantitative optical coherence tomography," Sci. Transl. Med. **7**(292), 292ra100 (2015).
19. M. Lenz, R. Krug, C. Dillmann, R. Stroop, N. C. Gerhardt, H. Welp, K. Schmieder, and M. R. Hofmann, "Automated differentiation between meningioma and healthy brain tissue based on optical coherence tomography ex vivo images using texture features," J. Biomed. Opt. **23**(07), 1 (2018).
20. K. Yashin, M. Karabut, V. Fedoseeva, A. Khalansky, L. Matveev, V. Elagin, S. Kuznetsov, E. Kiseleva, L. Y. Kravets, I. Medyanik, and N. Gladkova, "Multimodal optical coherence tomography in visualization of brain tissue structure at glioblastoma (experimental study)," Sovrem. Tehnol. Med. **8**(1), 73–81 (2016).
21. X. Yu, C. Hu, W. Zhang, J. Zhou, Q. Ding, M. Sadiq, Z. Fan, Z. Yuan, and L. Liu, "Feasibility evaluation of micro-optical coherence tomography (μOCT) for rapid brain tumor type and grade discriminations: μOCT images versus pathology," BMC Med. Imaging **19**(1), 1–12 (2019).
22. P. Strenge, B. Lange, C. Grill, W. Draxinger, V. Danicke, D. Theisen-Kunde, M. Bonsanto, R. Huber, and R. Brinkmann, "Ex vivo and in vivo imaging of human brain tissue with different OCT systems," in *European Conference on Biomedical Optics*, (Optical Society of America, 2019), 11078_11049.
23. K. S. Yashin, E. B. Kiseleva, E. V. Gubarkova, A. A. Moiseev, S. S. Kuznetsov, P. A. Shilyagin, G. V. Gelikonov, I. A. Medyanik, L. Y. Kravets, and A. A. Potapov, "Cross-polarization optical coherence tomography for brain tumor imaging," Front. Oncol. **9**, 201 (2019).
24. P. A. Valdes, D. W. Roberts, F.-K. Lu, and A. Golby, "Optical technologies for intraoperative neurosurgical guidance," FOC **40**(3), E8 (2016).
25. E. M. Lankenau, M. Krug, S. Oelckers, N. Schrage, T. Just, and G. Hüttmann, "iOCT with surgical microscopes: a new imaging during microsurgery," Adv. Opt. Technol. **2**(3), 233–239 (2013).
26. M. Finke, S. Kantelhardt, A. Schlaefer, R. Bruder, E. Lankenau, A. Giese, and A. Schweikard, "Automatic scanning of large tissue areas in neurosurgery using optical coherence tomography," Int. J. Med. Robotics Comput. Assist. Surg. **8**(3), 327–336 (2012).
27. H. Böhringer, E. Lankenau, F. Stellmacher, E. Reusche, G. Hüttmann, and A. Giese, "Imaging of human brain tumor tissue by near-infrared laser coherence tomography," Acta Neurochir. **151**(5), 507–517 (2009).

Biomedical Optics EXPRESS

28. E. D. SoRelle, D. W. Yecies, O. Liba, C. F. Bennett, C.-M. Graef, R. Dutta, S. S. Mitra, L.-M. Joubert, S. H. Cheshier, and G. A. Grant, "Wide-field dynamic monitoring of immune cell trafficking in murine models of glioblastoma," *bioRxiv*, 220954 (2017).
29. B. J. Vakoc, R. M. Lanning, J. A. Tyrrell, T. P. Padera, L. A. Bartlett, T. Stylianopoulos, L. L. Munn, G. J. Tearney, D. Fukumura, R. K. Jain, and B. E. Bouma, "Three-dimensional microscopy of the tumor microenvironment in vivo using optical frequency domain imaging," Nat. Med. **15**(10), 1219–1223 (2009).
30. N. Katta, A. D. Estrada, A. B. McElroy, A. Gruslova, M. Oglesby, A. G. Cabe, M. D. Feldman, R. D. Fleming, A. J. Brenner, and T. E. Milner, "Laser brain cancer surgery in a xenograft model guided by optical coherence tomography," Theranostics **9**(12), 3555–3564 (2019).
31. Y. Pan, J. You, N. D. Volkow, K. Park, and C. Du, "Ultrasensitive detection of 3D cerebral microvascular network dynamics in vivo," NeuroImage **103**, 492–501 (2014).
32. K. S. Yashin, E. B. Kiseleva, E. V. Gubarkova, L. A. Matveev, M. M. Karabut, V. V. Elagin, M. A. Sirotkina, I. A. Medyanik, L. Y. Kravets, and N. D. Gladkova, "Multimodal optical coherence tomography for in vivo imaging of brain tissue structure and microvascular network at glioblastoma," in *Clinical and translational neurophotonics*, (International Society for Optics and Photonics, 2017), 100500Z.
33. J. Zhu, S. P. Chong, W. Zhou, and V. J. Srinivasan, "Noninvasive, in vivo rodent brain optical coherence tomography at 2.1 microns," Opt. Lett. **44**(17), 4147–4150 (2019).
34. V. J. Srinivasan, A. C. Chan, and E. Y. Lam, "Doppler OCT and OCT angiography for in vivo imaging of vascular physiology," Selected Topics in Optical Coherence Tomography, 21 (2012).
35. M. Sato, K. Eto, J. Masuta, K. Inoue, R. Kurotani, H. Abe, and I. Nishidate, "In Vivo Rat Brain Imaging through Full-Field Optical Coherence Microscopy Using an Ultrathin Short Multimode Fiber Probe," Appl. Sci. **9**(2), 216 (2019).
36. K. S. Park, J. G. Shin, M. M. Qureshi, E. Chung, and T. J. Eom, "Deep brain optical coherence tomography angiography in mice: in vivo, noninvasive imaging of hippocampal formation," Sci. Rep. **8**(1), 11614 (2018).
37. Y. Li, W. J. Choi, W. Qin, U. Baran, L. M. Habenicht, and R. K. Wang, "Optical coherence tomography based microangiography provides an ability to longitudinally image arteriogenesis in vivo," J. Neurosci. Methods **274**, 164–171 (2016).
38. P. Shin, W. Choi, J. Joo, and W.-Y. Oh, "Quantitative hemodynamic analysis of cerebral blood flow and neurovascular coupling using optical coherence tomography angiography," J. Cereb. Blood Flow Metab. **39**(10), 1983–1994 (2019).
39. O. Liba, E. D. SoRelle, D. Sen, and A. de La Zerda, "Contrast-enhanced optical coherence tomography with picomolar sensitivity for functional in vivo imaging," Sci. Rep. **6**(1), 23337 (2016).
40. S. Tamborski, H. C. Lyu, H. Dolezyczek, M. Malinowska, G. Wilczynski, D. Szlag, T. Lasser, M. Wojtkowski, and M. Szkulmowski, "Extended-focus optical coherence microscopy for high-resolution imaging of the murine brain," Biomed. Opt. Express **7**(11), 4400–4414 (2016).
41. P. J. Marchand, D. Szlag, J. Extermann, A. Bouwens, D. Nguyen, M. Rudin, and T. Lasser, "Imaging of cortical structures and microvasculature using extended-focus optical coherence tomography at 1.3 µm," Opt. Lett. **43**(8), 1782–1785 (2018).
42. H. Dolezyczek, S. Tamborski, P. Majka, D. M. Sampson, M. Wojtkowski, G. Wilczynski, M. Szkulmowski, and M. Malinowska, "In vivo brain imaging with multimodal optical coherence microscopy in a mouse model of thromboembolic photochemical stroke," Neurophotonics **7**(01), 1 (2020).
43. J. A. Izatt, M. D. Kulkarni, S. Yazdanfar, J. K. Barton, and A. J. Welch, "In vivo bidirectional color Doppler flow imaging of picoliter blood volumes using optical coherence tomography," Opt. Lett. **22**(18), 1439–1441 (1997).
44. Z. Chen, T. E. Milner, S. Srinivas, X. Wang, A. Malekafzali, M. J. Van Gemert, and J. S. Nelson, "Noninvasive imaging of in vivo blood flow velocity using optical Doppler tomography," Opt. Lett. **22**(14), 1119–1121 (1997).
45. A. Holtmaat, T. Bonhoeffer, D. K. Chow, J. Chuckowree, V. De Paola, S. B. Hofer, M. Hübener, T. Keck, G. Knott, and W.-C. A. Lee, "Long-term, high-resolution imaging in the mouse neocortex through a chronic cranial window," Nat. Protoc. **4**(8), 1128–1144 (2009).
46. W. M. Wells, A. Colchester, and S. Delp, *Medical Image Computing and Computer-Assisted Intervention-MICCAI'98: First International Conference, Cambridge, MA, USA, October 11-13, 1998, Proceedings* (Springer, 2006).
47. E. Zudaire, L. Gambardella, C. Kurcz, and S. Vermeren, "A computational tool for quantitative analysis of vascular networks," PLoS One **6**(11), e27385 (2011).
48. V. Zuluaga-Ramirez, S. Rom, and Y. Persidsky, "Craniula: A cranial window technique for prolonged imaging of brain surface vasculature with simultaneous adjacent intracerebral injection," Fluids Barriers CNS **12**(1), 24 (2015).
49. M. M. Koletar, A. Dorr, M. E. Brown, J. McLaurin, and B. Stefanovic, "Refinement of a chronic cranial window implant in the rat for longitudinal in vivo two–photon fluorescence microscopy of neurovascular function," Sci. Rep. **9**(1), 5499 (2019).
50. S. Yang, K. Liu, H. Ding, H. Gao, X. Zheng, Z. Ding, K. Xu, and P. Li, "Longitudinal in vivo intrinsic optical imaging of cortical blood perfusion and tissue damage in focal photothrombosis stroke model," J. Cereb. Blood Flow Metab. **39**(7), 1381–1393 (2019).
51. S. Takano, "Glioblastoma angiogenesis: VEGF resistance solutions and new strategies based on molecular mechanisms of tumor vessel formation," Brain Tumor Pathol. **29**(2), 73–86 (2012).

Biomedical Optics EXPRESS

52. E. B. Kiseleva, K. S. Yashin, A. A. Moiseev, L. B. Timofeeva, V. V. Kudelkina, A. I. Alekseeva, S. V. Meshkova, A. V. Polozova, G. V. Gelikonov, and E. V. Zagaynova, "Optical coefficients as tools for increasing the optical coherence tomography contrast for normal brain visualization and glioblastoma detection," Neurophotonics **6**(03), 1 (2019).
53. D. Yecies, O. Liba, E. D. SoRelle, R. Dutta, E. Yuan, H. Vogel, G. A. Grant, and A. de la Zerda, "Speckle modulation enables high-resolution wide-field human brain tumor margin detection and in vivo murine neuroimaging," Sci. Rep. **9**(1), 10388 (2019).
54. H. Takahashi, K. Kato, K. Ueyama, M. Kobayashi, G. Baik, Y. Yukawa, J.-i. Suehiro, and Y. T. Matsunaga, "Visualizing dynamics of angiogenic sprouting from a three-dimensional microvasculature model using stage-top optical coherence tomography," Sci. Rep. **7**(1), 42426 (2017).
55. M. Parravano, L. Querques, F. Scarinci, P. Giorno, D. De Geronimo, R. Gattegna, M. Varano, F. Bandello, and G. Querques, "Optical coherence tomography angiography in treated type 2 neovascularization undergoing monthly anti-VEGF treatment," Acta Ophthalmol. **95**(5), e425–e426 (2017).
56. L. Kuehlewein, K. K. Dansingani, E. Talisa, M. A. Bonini Filho, N. A. Iafe, T. L. Lenis, K. B. Freund, N. K. Waheed, J. S. Duker, and S. R. Sadda, "Optical coherence tomography angiography of type 3 neovascularization secondary to age-related macular degeneration," Retina **35**(11), 2229–2235 (2015).